IEEE Photonics Journal
An IEEE Photonics Society Publication

Open Access

Ultra-Low Index-Contrast Polymeric Photonic Crystal Nanobeam Electro-Optic Modulator

Volume 12, Number 3, June 2020

Xiaogang Li
Xiao Liu
Yuqin Qin
Daquan Yang
Yuefeng Ji

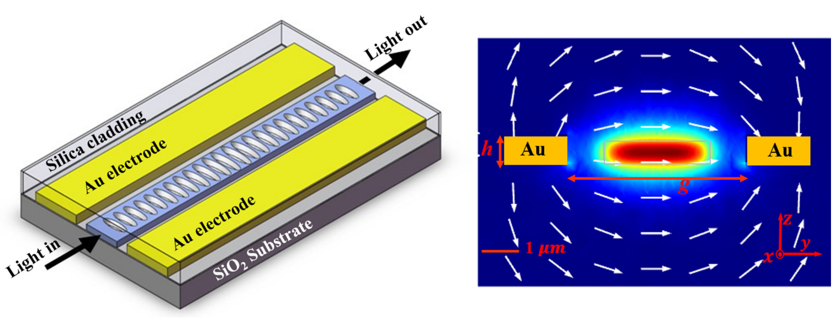

DOI: 10.1109/JPHOT.2020.2994241

Ultra-Low Index-Contrast Polymeric Photonic Crystal Nanobeam Electro-Optic Modulator

Xiaogang Li,[1] Xiao Liu,[1] Yuqin Qin,[2] Daquan Yang ,[1] and Yuefeng Ji [1]

[1]State Key Lab of Information Photonics and Optical Communications and School of Information and Communication Engineering, Beijing University of Posts and Telecommunications, Beijing 100876, China
[2]International School, Beijing University of Posts and Telecommunications, Beijing 100876, China

DOI:10.1109/JPHOT.2020.2994241

Manuscript received March 5, 2020; revised May 5, 2020; accepted May 8, 2020. Date of publication May 12, 2020; date of current version May 26, 2020. This work was supported in part by the National Natural Science Foundation of China (NSFC) under Grant 11974058, in part by the Fundamental Research Funds for the Central Universities under Grant 2018XKJC05, and in part by the Fund of the State Key Laboratory of Information Photonics and Optical Communications under Grant IPOC 2019ZT03, BUPT, China. Corresponding author: Daquan Yang (e-mail: yangdq5896@163.com).

Abstract: A novel nanocavity-based polymer-on-insulator (POI) electro-optic modulator (EOM) is proposed. It consists of a polymeric photonic-crystal nanobeam cavity (PCNC) with ultra-low index-contrast ($n_{cavity}/n_{bg} = 1.17$). Based on three-dimensional (3D) finite-difference time-domain (FDTD) method, the PCNC design and optimization are investigated theoretically. A high quality-factor (Q) of 3.4×10^4 and small mode-volume of 22.8 $(\lambda/n_{SEO})^3$ can be achieved. In order to judge the efficiency of the cavity design for electro-optic (EO) modulation, the optical modes and the electric field distribution are computed using an electromagnetic finite-element solver. Benefiting from the fast and strong EO effect in polymers, the modulator shows an EO modulation efficiency of up to 16 pm/V, which is over an order of magnitude higher than that in lithium niobate (LN) PCNCs. Moreover, the device is only 80 μm in length, leading to a voltage-length product $V_\pi \times L = 0.05$ V·cm, which is much smaller than those of Mach-Zehnder modulators. To the best of our knowledge, this is the first on-chip POI-based EOM that features both ultra-compact size and high modulation efficiency. Hence, it is potentially an ideal platform for applications in optical communications, electric-field sensing, and tunable photonic circuits.

Index Terms: Electro-optical systems, optical interconnects, photonic crystals, nanocavities, theory and design.

1. Introduction

On-Chip electro-optic modulators (EOMs) have been widely investigated during the past two decades for use in long-haul communication networks and short-reach optical interconnects [1]–[4]. Waveguide-based [5]–[7], Mach-Zehnder interferometer (MZI) [8]–[11], surface plasmon resonance (SPR) [12], [13], and optical microcavity EOMs [14]–[32] have all been developed. Optical microcavities with exceptional quality factor (Q) to mode volume (V) ratios (Q/V) have attracted particular interest, because of their strong ability to confine optical mode [33], [34]. Numerous EOMs based on optical microcavities have been proposed successively in recent years: microdisk cavities [14], [15], racetrack cavities [16], ring cavities [17], [18], Fabry-Pérot (F-P) cavities [19], [20], and photonic crystal (PhC) cavities [21]–[32]. Among these, PhC cavity-based EOMs, including 2D PhC cavities [21]–[24], and 1D PhC cavities [25]–[32], have emerged as promising platforms for low power and high efficiency operation due to their ultrahigh *Q/V* and compact size. Compared with 2D PhC cavities, 1D photonic crystal nanobeam cavities (PCNCs) have attracted great attention for use as EOMs due to their ultracompact footprints and convenient integration with bus-waveguides [35], [36], which are critical features for high density on-chip integration. Most reported PCNC-EOMs to date belong to the silicon-on-insulator (SOI) type, including Si-Doped [25] and Si-Graphene hybrid (SGH) modulators [26], [27]. However, SOI-based modulators rely on weak free carrier dispersion (which is inherently absorptive and nonlinear) rather than on the linear electro-optic (EO) effect (Pockels effect) [9]. To overcome the intrinsic absence of the Pockels effect in unstrained silicon, modulators based on combinations of silicon with Pockels-type material have been used, including Si-Organic hybrid (SOH) [28]–[30], and Si-Lithium niobate (SiLN) hybrid PCNC-EOMs [31], [32]. While these approaches have shown promising results, the reduced EO overlap between the electric field and the active material region degrades the modulation efficiency [17]. Fortunately, organic EO polymers are potential candidates for high efficiency modulators due to their high EO coefficients ($\sim$110 pm/V in the case of SEO100C [37]), low dielectric constants, ultrafast response time, and spin coating compatibility with many existing material platforms [3].

In this work, we present a polymer-on-insulator (POI) PCNC-EOM that features a compact footprint and ultrahigh modulation efficiency. The device layer consists of an EO polymer SEO100 C ($n_{cavity} = 1.699$); the substrate is silica ($n_{bg} = 1.45$). Based on three-dimensional (3D) finite-difference time-domain (FDTD) method (a commercial software package, Lumerical FDTD Solutions), the PCNC design and optimization are investigated theoretically. Despite an extraordinarily low index-contrast ($n_{cavity}/n_{bg} = 1.17$), a high *Q*-factor of 3.4 $\times 10^4$ and small mode volume of 22.8 $(\lambda/n_{SEO})^3$ can be achieved. In order to judge the efficiency of the device, the electric field distribution and the change of polymer refractive index are analyzed using 3D finite-element-method (FEM) (a commercial software package, COMSOL Multiphysics software). The result shows an EO modulation efficiency up to 16 pm/V, which is over an order of magnitude higher than that in lithium niobate (LN) PCNC [38]. Moreover, the total device length is only 80 μm, keeping the voltage-length product $V_\pi \times L$ as low as 0.05 V·cm. These results show that the POI-PCNC platform in this work offers an inexpensive, practical, and compact but high-performance alternative to conventional devices. Furthermore, the advanced performance of the on-chip POI EOM will play an important role in the future development of converged, collaborative and co-automatic optical network [39].

The rest of this paper is organized as follows. We start by introducing polymeric PCNC design in detail in Section 2. In Section 3, we describe design optimization and EO response for the polymeric PCNC-EOM. Finally, we present a brief conclusion in Section 4.

2. Cavity Design

The schematic of the ultra-low index-contrast ($n_{cavity}/n_{bg} = 1.17$) polymeric PCNC described in this paper is shown in Fig. 1(a). The cavity design is based on the deterministic high *Q*-factor method by Quan *et al.* [40]. The proposed polymeric PCNC consists of elliptical holes in decreasing dimensions, etched into a polymer ridge waveguides with a width of $w_{nb} = 3$ μm. The thickness of the polymer ridge waveguide is$h_{nb} = 550$ nm, and the periodicity of the elliptical holes is $a =$ 510 nm. The structure is symmetric with respect to the dark dashed line in Fig. 1(a). To create a Gaussian mirror [35], the elliptical-hole dimensions are linearly tapered from the center to both ends. In the taper region, the minor axes r_x decreases from 165 to 125 nm, and the major axes r_y decreases from 1.44 to 1.12 μm. The reason for choosing elliptical shape instead of circular shape is because elliptical holes have larger bandgap and higher reflectivity to confine the optical mode [41]. Fig. 1(b) shows the top view of the major field distribution along the polymeric PCNC. Fig. 2(a) and (b) show the lattice unit geometric parameters in the band diagram calculation and the transverse-electric (TE) band diagrams of the PCNC. Here, in order to display the photonic bandgap (PBG) in TE band clearly, only draw the first bands above and below the PBG (namely,

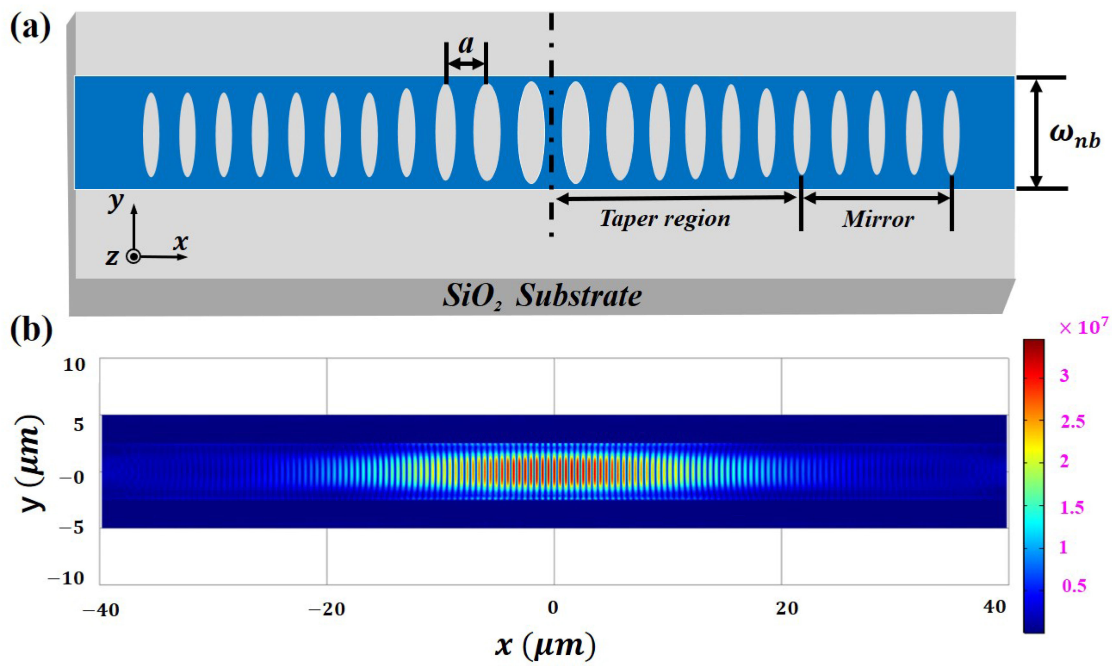

Fig. 1. (a) Schematic of the polymer-on-insulator 1D photonic crystal nanobeam cavity (PCNC). The structure is symmetric with respect to its center (the dark dashed line). (b) The major electric field (E_y) distributions along the 1D PCNC.

the air mode and dielectric mode for each air hole dimensions [40]), which are below the light line. And the other band curves above the light line for each air hole dimensions are not displayed in the TE band diagram [Fig. 2(b)]. The 3D-FDTD method with Bloch boundary conditions is utilized for the simulations. As expected, when the refractive index increases with the holes dimensions decreasing, the band of the structure moves to lower frequency. So the band for the structure with $r_x = 165$ nm, $r_y = 1440$ nm (red line) is higher than the one for $r_x = 125$ nm, $r_y = 1220$ nm (blue line). Here, the green dot in Fig. 2(b) indicates the target frequency 193.95 THz (1546.8 nm) of the proposed polymeric PCNC. Fig. 2(c) shows the calculated mirror strength γ for different filling fractions $f = (\pi \times r_x \times r_y)/(a \times w_{nb})$, where γ can be calculated by [35]:

$$\gamma = \sqrt{(\omega_2 - \omega_1)^2/(\omega_2 + \omega_1)^2 - (\omega_{res} - \omega_0)^2/\omega_0^2} \tag{1}$$

where ω_{res} is the target resonant frequency and ω_2, ω_1 and ω_0 are the air band edge, dielectric band edge, and mid-gap frequency of each segment, respectively [35]. As seen in Fig. 2(c), when $r_x = 125$ nm, the maximum mirror strength is obtained. Thus, the dimensions of the air-mode holes on both ends of tapering section $r_x = 125$ nm is chosen to build polymeric PCNC design.

At the end of this paragraph, Fig. 2(d) will be described. First, in order to design 1D polymeric PCNC achieving high Q-factor, the number of the taper segments N_t in the Taper section and the number of mirror segments N_m in the Mirror section are investigated in detail, respectively. As shown in Fig. 3(a), we investigate the influence of N_t (changed from $N_t = 30$ to $N_t = 170$) on the cavity Q-factor, and there is no additional mirror segments namely $N_m = 0$. As seen, with the N_t increasing, the cavity Q-factor increases. Herein, in order to save the simulation time of the transmission calculation [36], we use a low Q-factor geometry: N_t is selected as $N_t = 50$. Fig. 3(b) shows the calculated Q-factor as a function of N_m changed from $N_m = 0$ to $N_m = 90$, while N_t is kept fixed as $N_t = 50$. It can be seen that, with the increase of N_m, an optimized Q-factor of 3.4×10^4 can be obtained. In order to achieve a radiation-Q-limited cavity [35], [40], we place 50 taper segments in the Gaussian mirror region and 20 additional mirror segments on both ends.

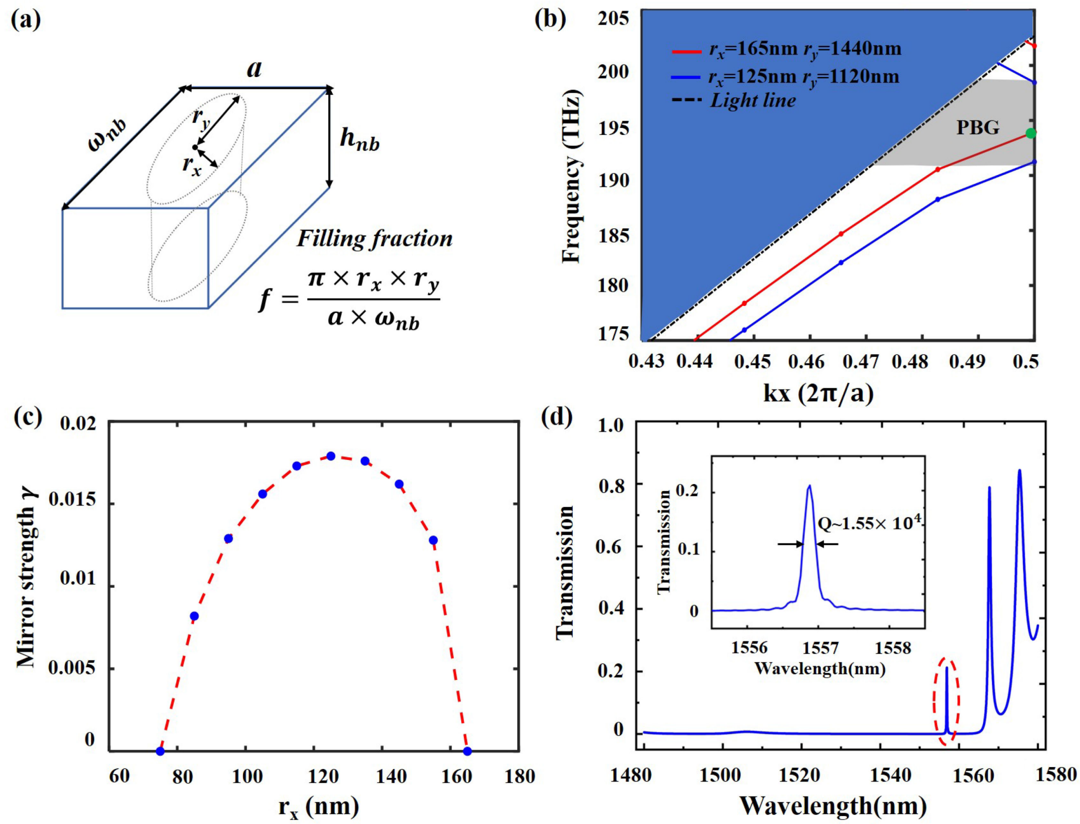

Fig. 2. (a) The lattice unit geometric parameters of the PCNC used in the band diagram calculation. (b) Transverse-electric band diagram for the polymeric PCNC. (c) Mirror strength γ obtained by using three-dimensional (3D) finite-difference time-domain (FDTD) simulation for different minor axes r_x. Other parameters are kept as in (a–b). (d) Transmission spectra of the optimized nanobeam cavity from 3D-FDTD simulation.

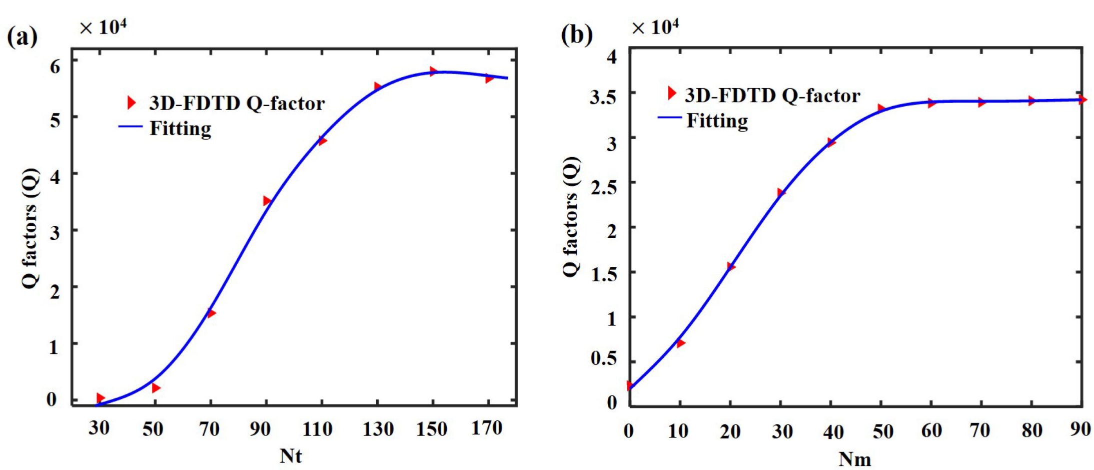

Fig. 3. (a) 3D-FDTD calculated Q-factor as a function of number of taper segments (with no mirror segments). (b) 3D-FDTD calculated Q-factor as a function of number of mirror segments (with 50 taper segments).

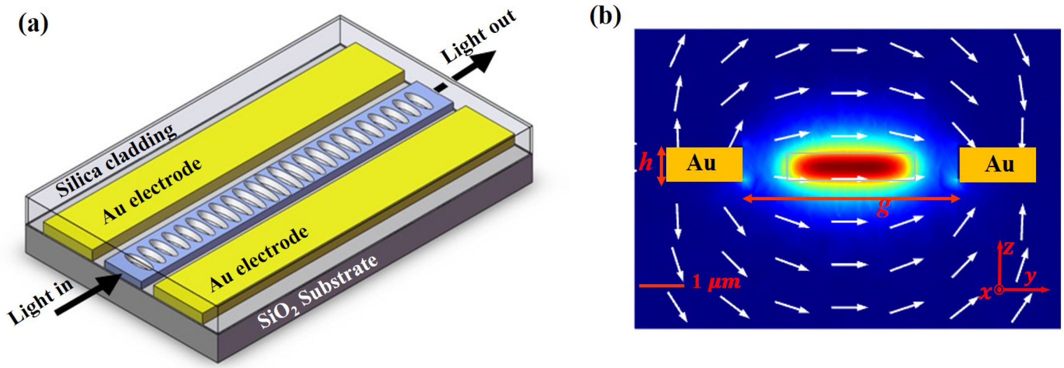

Fig. 4. (a) Schematic view of the modulator with polymeric PCNC and electrodes. The holes are filled with silica cladding. (b) The numerically calculated electro-optic overlap (cross sectional view). The optical mode electric field norm is plotted in color, and the applied electric field is shown by white arrows. *g:* gap between electrodes; *h:* electrode thickness.

Through the 3D-FDTD simulation of the optimal structure mentioned above, a fundamental mode at ∼1557 nm with a calculated *Q*-factor as high as 1.55×10^4 can be obtained [Fig. 2(d)]. Generally, for resonator-based EOM, the maximum modulation frequency can be affected by the cavity photon lifetime τ (proportional to *Q*), emphasizing that for modulation purposes the cavity *Q*-factor should not exceed 1.2×10^4 if a bandwidth of 100 GHz is desired [24], [42].

3. Electro-Optic Response

The configuration of the modulator in this work is presented in Fig. 4(a). By using a standard lift-off process to pattern gold electrode-free near the cavity optical mode, EO modulation can be achieved. To characterize the efficiency of our nanobeam cavity design for EO applications, we apply an external DC voltage. This changes the refractive index of the EO polymer, thereby modifying the resonance wavelength of the cavity. The wavelength shift $\Delta\lambda$ generated by a small permittivity perturbation $\Delta\varepsilon$ can be calculated by cavity perturbation theory [43], [44]. We know refractive index is given by $n=\sqrt{\mu\varepsilon}$. In the present case, the permeability $\mu=1$, and thus $\Delta\varepsilon\approx\varepsilon\cdot 2\Delta n/n$. Assuming a homogenous change of refractive index, the refractive index offset $\Delta n/n$ is alike everywhere in the perturbed region, and zero in the unperturbed region. Therefore, the resonance wavelength offset can be approximated as [43]:

$$\frac{\Delta\lambda}{\lambda}\approx-\frac{1}{2}\frac{\int_{\text{cavity}}\Delta\varepsilon|E|^2dV}{\int_V\varepsilon|E|^2dV}\approx-\frac{\Delta n}{n}\frac{\int_{\text{cavity}}|E|^2dV}{\int_V|E|^2dV} \tag{2}$$

where λ describes the resonant wavelength of the original cavity, and E represents the electric field of the unperturbed optical mode.

EO overlap between the corresponding TE optical modes and in-plane DC electric fields (E_y) interacting through the highest EO tensor component ($r_{33}\sim 110$ pm/V) is computed using an electromagnetic finite-element solver (a commercial software package, COMSOL Multiphysics software) [Fig. 4(b)]. In the simulation, the electrostatic field module, the electromagnetic wave, frequency domain, and the scattering boundary condition are chosen. Firstly, we change the electrode thickness h to find the relatively large average electric field [42]:

$$E_{\text{avg}}=\frac{\iiint E_{op}^2E_y\,dydzdx}{\iiint E_{op}^2\,dydzdx} \tag{3}$$

where E_{op} represents the optical field, and E_y describes the applied electric field. Obviously, thicker electrodes can make the EO interaction stronger [Fig. 5(a)]; considering the cost of the gold film,

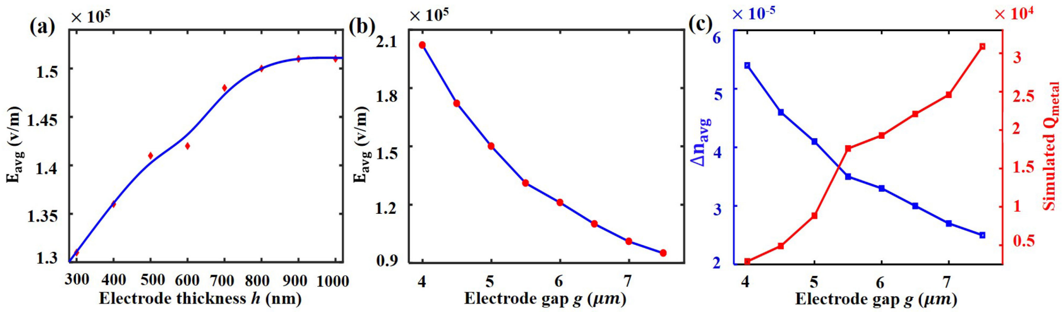

Fig. 5. (a) The average electric field increases as the electrode is thicker. Fixed electrode gap: 5 μm. (b) The average electric field decreases as the electrode gap is wider. Fixed electrode thickness: 0.8 μm; applied voltage: 1 V. (c) Plot showing how the simulated Δn_{avg} (left axis) and Q_{metal} (right axis) change with the increase of electrode gap.

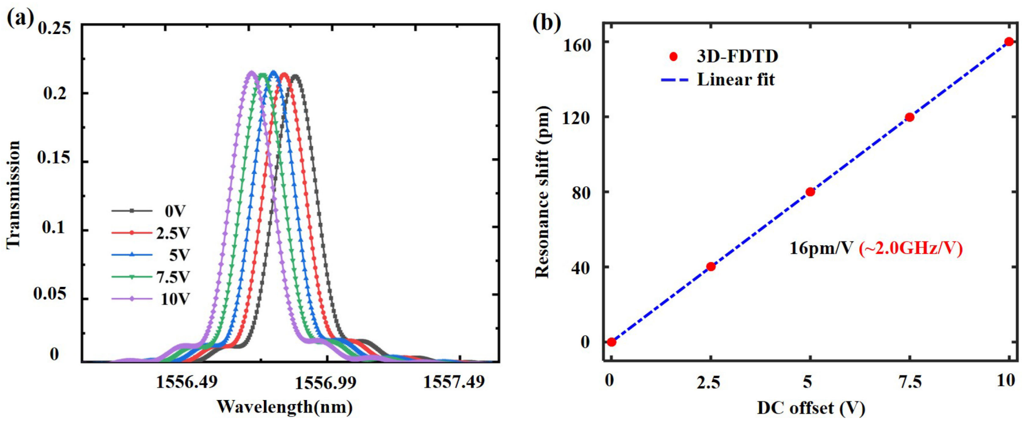

Fig. 6. (a) Simulated transmission spectra of polymeric PCNC for different applied voltages. (b) Resonant wavelength shift against applied voltage, showing a modulation efficiency of 16 pm/V.

we choose electrodes with a thickness of 800 nm. Then, the gap distance between the metal electrodes and the cavity is also a key design parameter in such a device. The simulation also suggests that E_{avg} inside the cavities falls off exponentially as the electrode gap g increases [Fig. 5(b)]. As expected, with the electrode gap decreases, the EO interaction becomes stronger and the metal absorption loss will increase. We define a loss parameter, Q_{metal}, to be the Q due only to absorption losses in the metal electrodes [31]. As seen, the Q_{metal} values increases as the electrode gap g increases [Fig. 5(c), red line]. Meanwhile, we calculate the effective average index perturbation Δn_{avg}, which is caused by the applied voltage, according to Pockels formula [42]:

$$\Delta n_{\text{avg}} = -\frac{1}{2} n^3 r_{33} E_{\text{avg}} \tag{4}$$

However, Δn_{avg} decreases as the electrode gap g increases [Fig. 5(c), blue line]. The simulations suggest that there exists an optimal gap for designing the present electrode structure at a certain acceptable metal-induced absorption loss.

The strong light confinement allows us to place the gold electrodes closer to the polymeric PCNC. Choosing a gap $g = 5$ μm, we plot the optical transmission spectra at various applied voltages, as shown in Fig. 6(a). As the voltage increases, the spectra shows no observable changes in the maximum transmission level (extinction ratio) and linewidth (Q). The resonance wavelength shows a linear relation with voltage, featuring a simulated EO modulation efficiency $\Delta\lambda/\Delta V$ of 16 pm/V

[Fig. 6(b)]; this agrees well with the result of 18 pm/V calculated based on cavity perturbation theory (Eqs. 2-4). The modulation efficiency is over an order of magnitude higher than the reported value 0.13 GHz/V (~1 pm/V) in LN PCNC [38]. To evaluate resonant modulator devices, the full width half maximum (FWHM) voltage V_{FWHM} is often used [24], [28], which corresponds to the voltage needed to shift the resonance by its spectral width at half maximum intensity. We estimate the V_{FWHM} of our device to be 6.25 V. We also notice using a higher-Q structure can reduce drive voltage to satisfy many practical applications which demands lower voltage. As a direct comparison with the MZI modulator, we also calculate the voltage-length product $V_{\pi} \times L$ of the proposed modulator, finding it to be 0.05 V·cm. This value is much smaller than previously reported for the larger size MZI modulator [8], [11], [16], [18], [45].

4. Conclusion

In summary, we have proposed theoretically and numerically a POI PCNC-based EOM in which the induced shift in the resonant wavelength of the cavity through electrical tuning of the refractive index of EO polymer is used to modulate the optical intensity. By changing the electrode thickness and gap distance to acquire the optimal overlap between the optical and electric fields, a modulation efficiency up to 16 pm/V and voltage-length product of 0.05 V·cm can be achieved. Because of the strong light confinement in the polymeric PCNC, the designed modulator entire length is only 80 μm. These results show that the proposed monolithically integrated POI-PCNC platform could become a cost-effective and practical solution to satisfy the growing demand for on-chip electric-field sensors, optical communications, and tunable photonic circuits.

References

[1] G. T. Reed, G. Mashanovich, F. Y. Gardes, and D. J. Thomson, "Silicon optical modulators," *Nat. Photon.*, vol. 4, no. 518, 2010.
[2] E. L. Wooten *et al.*, "A review of lithium niobate modulators for fiber-optic communications systems," *IEEE J. Sel. Top. Quantum Electron.*, vol. 6, no. 1, pp. 69–82, Jan./Feb. 2000.
[3] J. Liu, G. Xu, F. Liu, I. Kityk, X. Liu, and Z. Zhen, "Recent advances in polymer electro-optic modulators," *Rsc. Adv.*, vol. 5, no. 21, pp. 15784–15794, 2015.
[4] A. Boes, B. Corcoran, L. Chang, J. Bowers, and A. Mitchell, "Status and potential of lithium niobate on insulator (LNOI) for photonic integrated circuits," *Laser Photon. Rev.*, vol. 12, no. 4, 2018, Art. no. 1700256.
[5] S. Koeber, R. Palmer, M. Lauermann, and H. Yu, "Femtojoule electro-optic modulation using a silicon-Corganic hybrid device," *Light. Sci. Appl.*, vol. 4, no. 2, 2015, Art. no. e255.
[6] L. Alloatti, R. Palmer, S. Diebold, K. P. Pahl, C. Koos, and J. Leuthold, "100 GHz silicon-organic hybrid modulator," *Light. Sci. Appl.*, vol. 3, 2014, Art. no. e173.
[7] F. Qiu *et al.*, "Ultra-thin silicon/electro-optic polymer hybrid waveguide modulators," *Appl. Phys. Lett.*, vol. 107, 2015, Art. no. 123302.
[8] C. Wang *et al.*, "Integrated lithium niobate electro-optic modulators operating at CMOS compatible voltages," *Nature*, vol. 562, pp. 101–104, no. 2018.
[9] C. Kieninger *et al.*, "Ultra-high electro-optic activity demonstrated in a silicon-organic hybrid modulator," *Optica*, vol. 5, no. 6, pp. 739–748, 2018.
[10] M. Li, L. Wang, X. Li, X. Xiao, and S. Yu, "Silicon intensity Mach-Zehnder modulator for single lane 100 Gb/s applications," *Photon. Res.*, vol. 6, no. 2, pp. 109–116, 2018.
[11] M. He, M. Xu, Y. Ren, J. Jian, L. Liu, and X. Cai, "High-performance hybrid silicon and lithium niobate Mach-Zehnder modulators for 100 Gbit/s and beyond," *Nat. Photon.*, vol. 13, pp. 359–364, 2019.
[12] C. Haffner *et al.*, "Low-loss plasmon-assisted electro-optic modulator," *Nature*, vol. 556, no. 7702, 2018, Art. no. 483.
[13] M. Ayata *et al.*, "High-speed plasmonic modulator in a single metal layer," *Sci.*, vol. 358, no. 6363, pp. 630–632, 2017.
[14] J. Wang *et al.*, "High-Q lithium niobate microdisk resonators on a chip for efficient electro-optic modulation," *Opt. Express*, vol. 23, no. 18, pp. 23072–23078, 2015.
[15] M. R. Watts, W. A. Zortman, D. C. Trotter, R. W. Young, and A. L. Lentine, "Vertical junction silicon microdisk modulators and switches," *Opt. Express*, vol. 19, no. 22, pp. 21989–22003, 2011.
[16] C. Wang, M. Zhang, B. Stern, M. Lipson, and M. Loncar, "Nanophotonic lithium niobate electro-optic modulators," *Opt. Express*, vol. 26, no. 2, pp. 1547–1555, 2018.
[17] L. Chen, M. G. Wood, and R M. Reano, "12.5 pm/V hybrid silicon and lithium niobate optical microring resonator with integrated electrodes," *Opt. Express*, vol. 21, no. 22, pp. 27003–27010, 2013.
[18] K. Alexander *et al.*, "Nanophotonic Pockels modulators on a silicon nitride platform," *Nat. Commun*, vol. 9, 2018, Art. no. 3444.
[19] B. Schmidt, Q. Xu, and J. Shakya, "Compact electro-optic modulator on silicon-on-insulator substrates using cavities with ultra-small modal volumes," *Opt. Express*, vol. 15, no. 6, pp. 3140–3148, 2007.

[20] S. Meister *et al.*, "High-speed Fabry-Pérot optical modulator in silicon with 3-m diode," *IEEE J. Lightw. Technol*, vol. 33, no. 4, pp. 878–881, 2015.
[21] J. H. Wlbern, A. Petrov, and M. Eich, "Electro-optical modulator in a polymer-infiltrated silicon slotted photonic crystal waveguide heterostructure resonator," *Opt. Express*, vol. 17, no. 1, pp. 304–313, 2009.
[22] C. Y. Lin *et al.*, "Electro-optic polymer infiltrated silicon photonic crystal slot waveguide modulator with 23 dB slow light enhancement," *Appl. Phys. Lett.*, vol. 97, no. 9, 2010, Art. no. 194.
[23] B. Qi *et al.*, "Ultracompact electrooptic silicon modulator with horizontal photonic crystal slotted slab," *IEEE Photon. Technol. Lett.*, vol. 22, no. 10, pp. 724–726, 2010.
[24] J. M. Brosi, C. Koos, L. C. Andreani, J. Leuthold, and W. Freude, "High-speed low-voltage electro-optic modulator with a polymer-infiltrated silicon photonic crystal waveguide," *Opt. Express*, vol. 16, no. 6, pp. 4177–4191, 2008.
[25] J. Hendrickson, R. Soref, J. Sweet, and W. Buchwald, "Ultrasensitive silicon photonic-crystal nanobeam electro-optical modulator: design and simulation," *Opt. Express*, vol. 22, no. 3, pp. 3271–3283, 2014.
[26] T. Pan *et al.*, "Analysis of an electro-optic modulator based on a graphene-silicon hybrid 1D photonic crystal nanobeam cavity," *Opt. Express*, vol. 23, no. 18, 2015, Art. no. 23357.
[27] H. Liu, P. Liu, L. Bian, C. Liu, Q. H. Zhou, "Electro-optic modulator side-coupled with a photonic crystal nanobeam loaded graphene/Al2O3 multilayer stack," *Opt. Mater. Express*, vol. 8, no. 4, pp. 761–774, 2018.
[28] B. Qi, P. Yu, Y. Li, X. Jiang, M. Yang, and J. Yang, "Analysis of electrooptic modulator with 1-D slotted photonic crystal nanobeam cavity," *IEEE Photon. Technol. Lett*, vol. 23, no. 14, pp. 992–994, 2011.
[29] S. Inoue and A. Otomo, "Electro-optic polymer/silicon hybrid slow light modulator based on one-dimensional photonic crystal waveguides," *Appl. Phys. Lett*, vol. 103, 2013, Art. no. 171101.
[30] H. Yan, X. Xu, and C. J. Chung, "One-dimensional photonic crystal slot waveguide for silicon-organic hybrid electro-optic modulators," *Opt. Lett.*, vol. 41, no. 23, pp. 5466–5469, 2016.
[31] J. D. Witmer, J. T. Hill, and A. H. Safavi-Naeini, "Design of nanobeam photonic crystal resonators for a silicon-on-lithium-niobate platform," *Opt. Express*, vol. 24, no. 6, pp. 5876–5885, 2016.
[32] J. D. Witmer, J. A. Valery, and P. Arrangoiz-Arriola, "High-Q photonic resonators and electro-optic coupling using silicon-on-lithium-niobate," *Sci. Rep.*, vol. 7, 2017, Art. no. 46313.
[33] D. Yang *et al.*, "Real-time monitoring of hydrogel phase transition in an ultrahigh Q microbubble resonator," *Photon. Res.*, vol. 8, no. 4, pp. 497–502, 2020.
[34] D. Yang *et al.*, "Packaged microbubble resonator for versatile optical sensing," *J. Lightw. Technol.*, doi: 10.1109/JLT.2020.2988206.
[35] Q. Quan, P. B. Deotare, and M. Loncar, "Photonic crystal nanobeam cavity strongly coupled to the feeding waveguide," *Appl. Phys. Lett*, vol. 96, 2010, Art. no. 203102.
[36] D. Yang, H. Tian, Y Ji, and Q. Quan, "Design of simultaneous high-Q and high-sensitivity photonic crystal refractive index sensors," *JOSA B*, vol. 30, no. 8, pp. 2027–2031, 2013.
[37] Y. Enami, J. Luo, and A. K. Jen, "Short hybrid polymer/sol-gel silica waveguide switches with high in-device electro-optic coefficient based on photostable chromophore," *AIP Advances*, vol. 1, no. 4, 2011, Art. no. 042137.
[38] Y. Li, C. Wang, and M. Loncar, "Design of nano-groove photonic crystal cavities in lithium niobate," *Opt. Lett*, vol. 40, no. 12, pp. 2902–2905, 2015.
[39] Y. Ji, J. Zhang, X. Wang, and H. Yu, "Towards converged, collaborative and co-automatic (3 C) optical networks," *Sci. China Inf. Sci.*, vol. 61, no. 12, 2018, Art. no. 121301.
[40] Q. Quan and M. Loncar, "Deterministic design of high Q small mode volume photonic crystal nanobeam cavities," *Opt. Express*, vol. 19, pp. 18 529–18 542, 2011.
[41] Q. Quan, I. B. Burgess, S. K. Tang, D. L. Floyd, and M. Loncar, "High-Q, low index-contrast polymeric photonic crystal nanobeam cavities," *Opt. Express*, vol. 19, pp. 22 191–22 197, 2011.
[42] C. Xiong, W. H. P. Pernice, and H. X. Tang, "Low-loss, silicon integrated, aluminum nitride photonic circuits and their use for electro-optic signal processing," *Nano Lett.*, vol. 12, no. 7, pp. 3562–3568, 2012.
[43] J. D. Joannopoulos, S. G. Johnson, J. N. Winn, and R. D. Meade, *Photonic Crystals, Molding the Flow of Light*. Princeton, NJ, USA: Princeton Univ. Press, 2011.
[44] S. G. Johnson, M. Ibanescu, M. A. Skorobogatiy, O. Weisbergs, J. D. Joannopoulos, and Y. Fink, "Perturbation theory for Maxwells equations with shifting material boundaries," *Phys. Rev. E*, vol. 65, 2002, Art. no. 066611.
[45] B. Desiatov, A. Shams-Ansari, M. Zhang, C. Wang, and M. Loncar, "Ultra-low-loss integrated visible photonics using thin-film lithium niobate," *Optica*, vol. 6, no. 3, pp. 380–384, 2019.